

## **Influence of decalcification on structural and mechanical properties of synthetic calcium silicate hydrate (C-S-H)**

Lin Liu <sup>a,b</sup>, Can Sun <sup>a</sup>, Guoqing Geng <sup>c,\*</sup>, Pan Feng <sup>d</sup>, Jiaqi Li <sup>e</sup>, Rainer Dähn <sup>c</sup>

<sup>a</sup> College of Civil and Transportation Engineering, Hohai University, Nanjing 210098, China

<sup>b</sup> Jiangsu Research Institute of Building Science Co., LTD., Nanjing 210008, China

<sup>c</sup> Laboratory of Waste Management, Paul Scherrer Institut, 5232 Villigen PSI, Switzerland

<sup>d</sup> Jiangsu Key Laboratory of Construction Materials, School of Materials Science and Engineering, Southeast University, Nanjing 211189, China

<sup>e</sup> Department of Civil and Environmental Engineering, University of California, Berkeley, CA 94720, USA

\* Corresponding author. Email address: [guoqing\\_geng@psi.ch](mailto:guoqing_geng@psi.ch).

### **Abstract**

Decalcification causes critical degradation of calcium silicate hydrate (C-S-H) – the principal binder in concrete. Contrary to structural change, the decalcification-induced change of C-S-H mechanical properties has not been sufficiently investigated. To fill this gap, here C-S-H was synthesized and decalcified using  $\text{NH}_4\text{NO}_3$  solutions. It was then subjected to chemical analysis and high pressure X-ray diffraction study. Our results indicate that C-S-H decalcifies only in the interlayer which reduces its stiffness along the *c*-axis. The incompressibility and the transverse isotropy remain unchanged for the calcium silicate main layer, despite the vast change of silicate chain linkage. The intralayer Ca does not leach as long as C-S-H maintains the tobermorite-like structure. A ~30% reduction of

bulk modulus is estimated for decalcified C-S-H. Our results add fundamental knowledge to the structure-property correlation of C-S-H subjected to decalcification.

**Keywords:** Calcium silicate hydrate; Decalcification; Mechanical properties; Molecular configuration; High pressure X-ray diffraction.

## 1. Introduction

C-S-H, the main hydration product of Portland cement, is responsible for most of the critical engineering properties of concrete [1-3]. Among all the degradation of C-S-H during the service life, one of the most commonly observed phenomena is the leaching-out of calcium when concrete structures are in contact with soft water or corrosive solutions [4]. This process, also termed decalcification, significantly alters the structure and binding ability of C-S-H, therefore making it a fundamental topic in studying the durability of concrete structures.

Studies on the influence of decalcification to the microstructure [5-11] and the volumetric stability [6] have been extensively reported. The polymerization degree of silicate chains in C-S-H changes during decalcification, which has been studied with  $^{29}\text{Si}$  Nuclear Magnetic Resonance (NMR) [11-13]. A silicate tetrahedron is expressed as  $Q^n$  when it shares  $n$  oxygen atoms with its neighbor silicate/aluminate tetrahedra. The average polymerization degree and mean chain length ( $MCL$ ) of silicate chains in C-S-H can be calculated from the integrated areal fractions of  $Q^n$  peaks on the  $^{29}\text{Si}$  NMR spectra ( $n=0,1,2,3,4$ ). It is universally reported that the average polymerization degree and  $MCL$  of C-S-H increase when Ca/Si ratio decreases [7, 14, 15]. As reported from the literature, the Ca/Si ratio of decalcified C-S-H can be as low as 0.2, leaving a doubt whether the decalcification takes place in both the interlayer and the intralayer, as such low Ca/Si ratios have never been reported from directly synthesized C-S-H.

In the meantime, Constantinides and Ulm investigated elastic properties of cement-based materials by nanoindentation tests on cement paste before and after calcium leaching [16]. They found that indentation modulus of low-density (LD) C–S–H drops from 21.7 GPa to 3.0 GPa, and indentation modulus of high-density (HD) C–S–H drops from 29.4 GPa to 12.0 GPa after cement paste was placed in 6 mol/L  $\text{NH}_4\text{NO}_3$  for 5 months. Similar results were reported for Ca-leached C-S-H from the hydration of ordinary Portland cement containing 6 wt.% nano-silica [17]. While providing the mechanical property at the scale of nanometer and a few microns, these studies did not report the mechanical property of the decalcified C-S-H layer structure that contains no extrinsic porosity between the solid domain. Such information is a fundamental input to model the multi-scale property of a leached cementitious matrix.

The mechanical property of pore-free C-S-H solid has been reported using molecular simulation [18, 19]. Only until recently, direct measurement of the anisotropic mechanical property of C-S-H is reported [20, 21]. High pressure X-ray diffraction (HP-XRD) evidences demonstrated that the incompressibility of C-S-H nanocrystals is dominated by the interlayer densification. This work opens the possibility to study the nanomechanical property evolution of decalcified C-S-H, and to correlate the property with the changing atomistic configuration. In this study, lab-synthesized C-S-H (I) was equilibrated in  $\text{NH}_4\text{NO}_3$  solution of different concentration to reach various degrees of decalcification. The chemical compositions of the samples before and after decalcification were determined by Rietveld refinement using lab-XRD data coupled with  $^{29}\text{Si}$  NMR measurement and Inductively Coupled Plasma Atomic Emission Spectroscopy (ICP-AES) data. Anisotropic mechanical properties of the samples were studied by HP-XRD measurement, which were then correlated to the molecular configurations of C-S-H. The results provide a direct link

between the atomistic structure and anisotropic stiffness of C-S-H subjected to decalcification.

## **2. Methodology**

### **2.1 C-S-H preparation and decalcification**

SiO<sub>2</sub> (Aerosil 200, Evonik), CaO (obtained by burning CaCO<sub>3</sub> (Merck Millipore) at 1000°C for 12 h) and deionized water were mixed at an initial bulk Ca/Si molar ratio of 1.4 and a water-to-solid mass ratio of 50 in a N<sub>2</sub>-filled glove box [22-24]. The mixtures were stored in Teflon bottles and cured at 80 °C for 92 days, then cured at room temperature for 215 days. The mixtures were filtered using 0.45 µm nylon filters paper at N<sub>2</sub> atmosphere, and then the C-S-H solids were dried in vacuum desiccators in the presence of saturated CaCl<sub>2</sub> solutions.

NH<sub>4</sub>NO<sub>3</sub> solution of 6 mol/L is often utilized as leaching agent to decalcify C-S-H in a relatively short time [10, 25, 26]. Our previous study indicates that the decalcification ability of NH<sub>4</sub>NO<sub>3</sub> solution increases with its concentration [27]. Here, the C-S-H powders were immersed in NH<sub>4</sub>NO<sub>3</sub> solution of different concentrations for extended time periods to obtain homogeneously decalcified C-S-H particles. In details, each 5 g C-S-H was immersed for 24 h in 150 mL NH<sub>4</sub>NO<sub>3</sub> solution of 0.5 mol/L, 1 mol/L and 4 mol/L, respectively. The suspensions were vacuum filtered using 0.45 µm nylon filter after 5 min hand shaking. The solids were then rinsed with deionized water and ethanol, followed by storage in N<sub>2</sub>-filled desiccators in the presence of CaCl<sub>2</sub> powders. C-S-H powders immersed in NH<sub>4</sub>NO<sub>3</sub> solution of 0.5 mol/L, 1 mol/L and 4 mol/L are denoted as D0.5, D1, D4, respectively; the C-S-H sample before leaching is denoted as D0. We did not intend to measure the mass after leaching, since an uncontrollable amount of powders might retain on the filter paper.

## 2.2 Chemical analysis

Ca/Si ratios of these powders were measured by ICP-AES. Each 0.1 g sample was mixed with LiBO<sub>3</sub> flux of 0.6 g and heated to 950°C for 25 min in a graphite crucible, vitrifying the sample to form clear beads. After cooling to room temperature, beads were placed in dilute HCl and heated until they were dissolved. The elemental Ca and Si concentrations in the resulting solutions were measured using ICP-AES.

<sup>29</sup>Si magic-angle spinning (MAS) NMR experiments were performed on an *Agilent 600 DD2* spectrometer at a resonance frequency of 119.23 MHz. <sup>29</sup>Si NMR cross polarization spectra were recorded with spinning rate of 15 kHz with a 4 mm probe at room temperature. Approximately 5,000 scans were performed on each sample. The spectra were deconvoluted using a mixed Lorentz (0.8)-Guass (0.2) peak profile. Using the calculated intensity fractions of  $Q^n$ , the average polymerization degree of C-S-H ( $n_c$ ) is calculated as [23]

$$n_c = \frac{Q^1 + 2Q^2 + 3Q^3}{Q^1 + Q^2 + Q^3} \quad (1)$$

The mean chain length ( $MCL$ ) is calculated as [23, 28]

$$MCL = \begin{cases} 2 \left( 1 + \frac{Q^2}{Q^1} \right) & (noncrosslinked) \\ 4 \left( 1 + \frac{Q^2 + Q^3}{Q^1} \right) & (crosslinked) \end{cases} \quad (2)$$

## 2.3 Quantitative analysis based on the lab-XRD data

The lab-XRD was conducted using a *Bruker-AXS D8 Advance* diffractometer. For each sample, ~1 g of powder was packed in a stainless-steel holder with a low-background supporter. Cu anode was used with the  $K\alpha$  emission wavelength to be ~1.54 Å. The 2 $\theta$  scanning range was between 2° and 70°, corresponding to a  $d$ -range of 43.9 Å – 1.34 Å. The step size was 0.01° and the scanning speed was 1°/min.

Rietveld refinement was conducted using the lab-XRD data and the MAUD package [29]. The experimental condition (lab-XRD with Cu anode) was pre-defined in the software. As will be shown later, three (nano)crystalline phases were identified in all the samples, i.e. C-S-H, jennite and calcite. The reported crystal structure of jennite [30] and calcite [31] were used as input phase models. Multiple crystal structures have been proposed for C-S-H (I) [32] as defected versions of tobermorite [33, 34], although they were validated to be generally all suitable models for the Rietveld refinement of C-S-H (I) [20]. This is mainly because of the nano-crystallinity of C-S-H (I) that results in limited number of broad diffraction peaks, which limits the refinement of occupancy and position of single atoms [35, 36]. For simplicity purpose, here we used the 11 Å tobermorite model (space group *B11m* [33]) for C-S-H (I) due to the similarity in basal spacing. Note that the usage of this model does not indicate any cross-linking in the structure. The crystallite size (pre-defined in MAUD) of all phases were allowed to be refined [21]. The degree of structural disorder was accounted by refining the ‘micro-strain’ parameters in the MAUD package, which contributes to the further peak broadening [29]. The background was refined using a 5<sup>th</sup>-order-polynomial, and the dominant air scattering at low angle ( $<5^\circ$ ) was accounted by refining a pseudo-Voigt peak function. The broad diffraction peak of amorphous silica (from  $15^\circ$  to  $30^\circ$ ) is also accounted by refining a pseudo-Voigt peak. The core information to be refined is the mass ratio between C-S-H, jennite and calcite. The mass percentage of amorphous gel was not intended to be investigated by XRD.

## **2.4 High pressure X-ray diffraction**

The HP-XRD experiment was conducted at beamline I15 of the DIAMOND Light Source, using an axial geometry set-up. A Le Toullec type membrane diamond anvil cell was used [37], with a diamond cutlet diameter of  $\sim 500\ \mu\text{m}$ . Gaskets were made from stainless steel

by drilling cylindrical chamber of  $\sim 200\ \mu\text{m}$  in diameter and  $\sim 80\ \mu\text{m}$  in thickness. Ethanol (80 vol.%) methanol (20 vol.%) solution was used as pressure medium. The incident X-ray beam energy was 29.2 keV, corresponding to a wavelength of  $0.4246\ \text{\AA}$ . The incident beam diameter was  $\sim 70\ \mu\text{m}$  to maximize the signal-to-noise ratio. A *MAR345* image plate was placed  $\sim 310.75\ \text{mm}$  downstream from the sample, resulting in an angular resolution of  $\sim 0.2^\circ$  at small angle and  $\sim 0.1^\circ$  at large angle. A  $2\theta$  range of  $\sim 1^\circ - \sim 20^\circ$  was covered, corresponding to a  $d$ -range of  $24.33\ \text{\AA} - 1.22\ \text{\AA}$ .

Due to the limited experiment time in synchrotron facility, only D0, D0.5 and D4 were measured. For each sample, 2D diffraction images were collected at 6-8 pressure points from ambient pressure to  $\sim 8\ \text{GPa}$ , loaded with helium gas loading equipment. The pressure values were calibrated using a Ruby fluorescence system. The diffraction images were processed to usual diffractogram using the Dioptas package [38]. The analysis of the diffractogram was conducted using XFIT [39]. Instead of a full-pattern Rietveld refinement, here peaks were fitted individually since the diffraction peaks of C-S-H (I) are rare and each well-indexed [20, 35, 36]. Besides, the key interest here is merely the  $d$ -values of each peak as a function of the applied pressure. Although pseudo-Voigt is usually used for XRD peak-fitting, we noticed that it required significant adjustment of peak-parameters for data at high pressure values, and sometimes resulted in peak positions that are unphysically deviated the trend line. On the contrary, Gaussian-fitting resulted in more reasonable peak positions, and therefore used in our analysis.

### 3. Results

#### 3.1 Lab-XRD data and the quantitative analysis results

The lab-XRD results are shown in Figure 1a. In sample D0 and D0.5, sharp diffractions near  $1/d \sim 0.096\ \text{\AA}^{-1}$ ,  $0.155\ \text{\AA}^{-1}$  and within the range from  $0.28\ \text{\AA}^{-1}$  to  $0.4\ \text{\AA}^{-1}$  indicate the

presence of jennite [30]. The Miller indices of the jennite peaks are labeled in Figure 1a. Note that they are no longer observed in sample D1 and D4. Diffraction peaks of calcite are also identified for all samples at  $1/d \sim 0.33 \text{ \AA}^{-1}$ ,  $0.40 \text{ \AA}^{-1}$ ,  $0.44 \text{ \AA}^{-1}$ ,  $0.48 \text{ \AA}^{-1}$ ,  $0.523 \text{ \AA}^{-1}$  and  $0.536 \text{ \AA}^{-1}$ , corresponding to Miller indices (104), (110), (113), (202), (018) and (116). The presence of calcite is most pronounced in D4, whereas nearly unobserved in D0. A diffused diffraction peak of amorphous silica is observed in D4, within the  $1/d$  range between  $0.2 \text{ \AA}^{-1}$  and  $0.35 \text{ \AA}^{-1}$ . Diffraction peaks of Portlandite (CH) are not observed in any samples here, although it is often reported to be present in the synthesis of C-S-H [3, 7, 8, 22]. This is mainly due to the elevated synthesis temperature in the current study that favors the precipitation of jennite.

Apart from all the sharp peaks of jennite and calcite, the unique diffraction of C-S-H significantly contributes to the XRD of all samples. As well documented in many publications [20, 35, 36], the diffraction pattern of C-S-H is characterized by 5-7 broad diffraction peaks that can be indexed according to the tobermorite structure. As shown in Figure 1a, using an  $11 \text{ \AA}$  tobermorite model with  $B11m$  symmetry, the strongest C-S-H peak near  $0.324 \text{ \AA}^{-1}$  is assigned to the (020) and  $(2\bar{2}0)$  reflections. The peaks near  $0.356 \text{ \AA}^{-1}$ ,  $0.547 \text{ \AA}^{-1}$  and  $0.598 \text{ \AA}^{-1}$  are assigned to (200),  $(2\bar{4}0)$  and  $(4\bar{2}0)$  reflections, respectively. Note that the presence of only  $(hk0)$  peaks, or  $hk$  bands as elsewhere termed [40], is due to the limited crystallite size and stacking disorder of C-S-H layer structure along the  $c$ -axis, which result in a broad (002) diffraction near  $1/d = 0.09 \text{ \AA}^{-1}$  (Figure 1a).



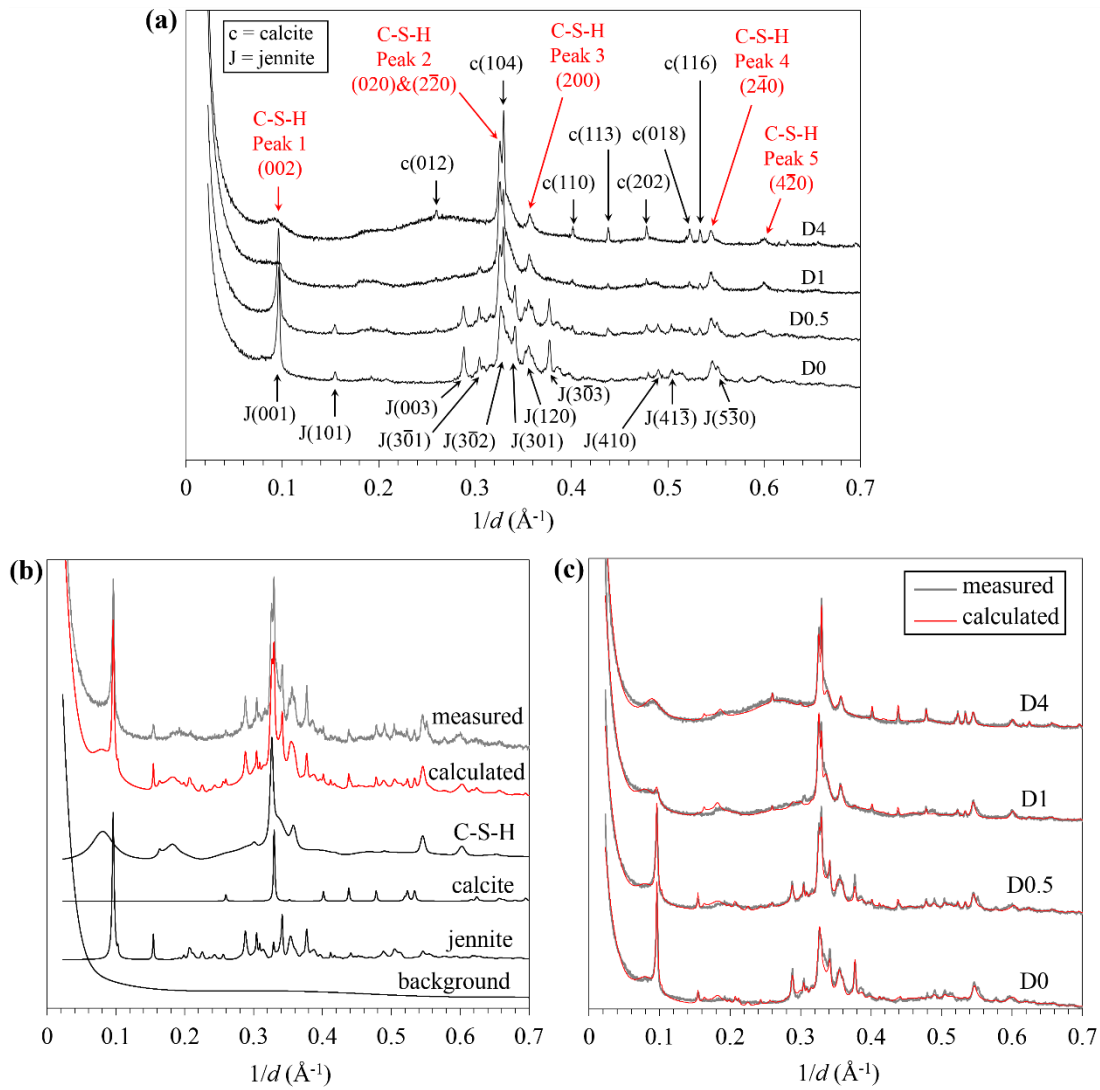


Figure 1. XRD results and quantitative analysis. (a) Lab experiment data with diffraction peaks indexed; (b) the calculated contributions from different phases, using the refinement of XRD of D0.5 as an example; (c) calculated diffraction of all samples plotted with the experiment data.

Rietveld refinement using the lab-XRD data calculates the contribution of each phase to the overall diffraction. An example (D0.5) is given in Figure 1b. The refinement was conducted on each sample, with satisfactory fit obtained between the calculated and measured XRD, as shown in Figure 1c. The refined phase components are listed in Table 1. C-S-H is the dominant phase in all samples while the jennite content is also significant

in D0 and D0.5. Calcite content is insignificant in D0, D0.5 and D1, yet becomes significant in D4. Note that the amorphous silica gel produced from decalcification is accounted in the background, and not counted in the total mass in Table 1.

Table 1. The refined mass percentage of jennite, calcite and C-S-H with respect to the summed mass of (nano)crystalline phases; error estimated to be ~1.5 % for jennite and calcite, and ~3 % for C-S-H.

Sample	jennite	calcite	C-S-H
D0	25.4%	2.4%	72.2%
D0.5	28.6%	5.8%	65.6%
D1	7.7%	4.0%	88.3%
D4	0	14.1%	85.9%

### 3.2. $^{29}\text{Si}$ NMR and ICP-AES study

The  $^{29}\text{Si}$  NMR spectra and their deconvoluted peaks are shown in Figure 2. Previous investigations on solid silicates have established the following assignments according to  $^{29}\text{Si}$  chemical shift ranges:  $Q^1$  at -76 to -82 ppm,  $Q^2$  at -82 to -88 ppm,  $Q^3$  at -88 to -104 ppm, and  $Q^4$  at -104 to -120 ppm [41, 42]. The  $Q^2$  peak has a shoulder near -84 ppm, which represents bridging tetrahedra ( $Q_b^2$ ), while the peak near -88 ppm represents paired tetrahedra ( $Q_p^2$ ). According to [28], in a non-crosslinked C-S-H the content of  $Q_p^2$  is theoretically twice that of  $Q_b^2$ . The relatively sharp diffraction peaks of jennite (Figure 1b) indicate at least micro-crystallinity. It is therefore reasonable to assume its Si species to be only  $Q_p^2$  and  $Q_b^2$ , also in a ratio of 2:1. The constraint that  $Q_p^2 : Q_b^2 = 2:1$  was thus applied in the spectra deconvolution for D0 and D0.5, which are non-crosslinked as indicated by the absence of  $Q^3$  peak. As for D1 and D4, the ratio between  $Q_p^2$  and  $Q_b^2$  is not fixed during deconvolution, since some bridging site of C-S-H may be accounted as  $Q^3$  when they are crosslinked. If  $Q_{b\_CSH}^2$  is less than half of  $Q_{p\_CSH}^2$ , the percentage of  $Q^3$  from C-S-H is determined as  $Q_{CSH}^3\% = 0.5 \times Q_{p\_CSH}^2\% - Q_{b\_CSH}^2\%$ , so that the amount of bridging

silicate is half the amount of paired silicate in C-S-H. The deconvolution result is shown in Table 2, with an error of ~1%.

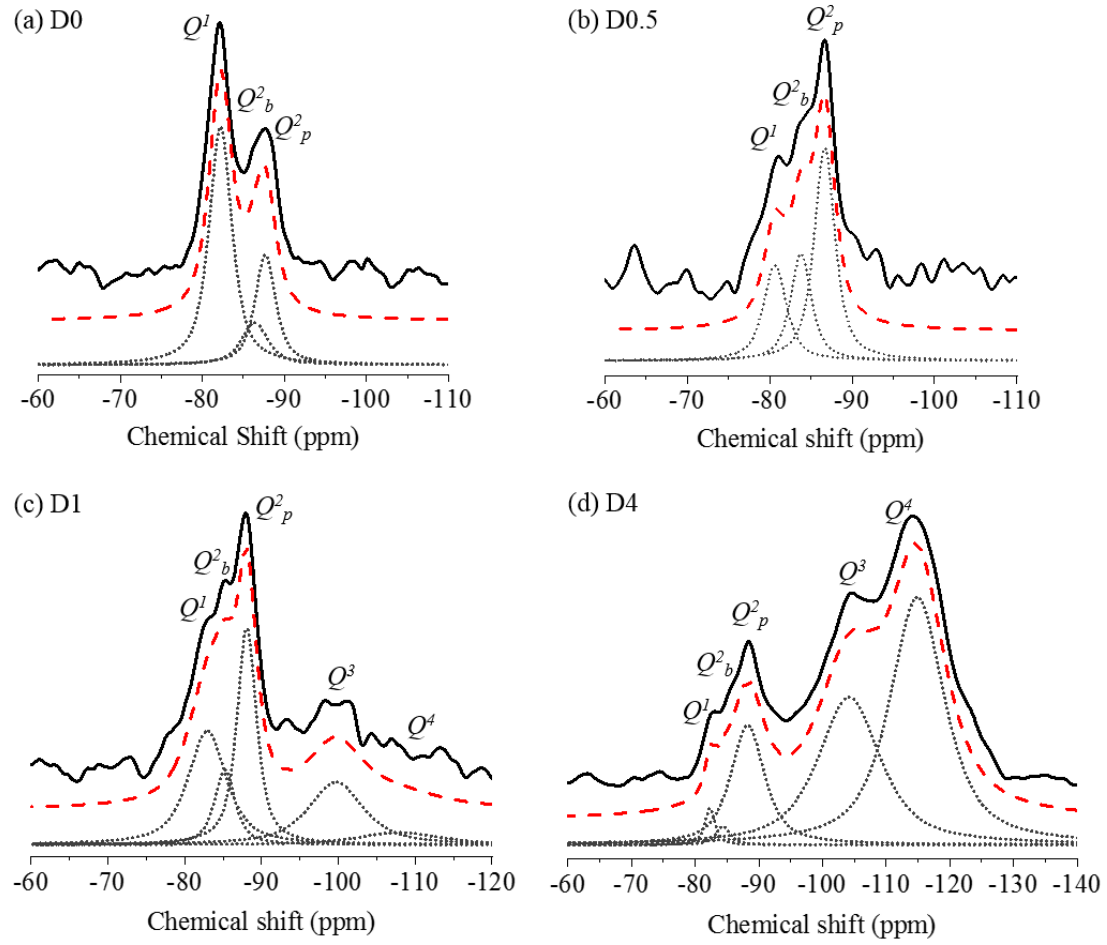


Figure 2.  $^{29}\text{Si}$  NMR spectra of (a) D0, (b) D0.5, (c) D1 and (d) D4 samples. The solid lines are the measured results. The black-dotted lines are fitted results of individual species, which add up to the red-dashed lines. Vertical offsets are applied for viewing convenience.

Table 2. The percentage of various silicate species obtained from deconvoluting the NMR results, with peak-fitting error ~1%.

Sample	$Q^1$ %	$Q^2_p$ %	$Q^2_b$ %	$Q^3$ %	$Q^4$ %
D0	61.4	25.8	12.9	0	0
D0.5	24.7	50.2	25.1	0	0
D1	29.7	29.1	10.5	23.7	7.1
D4	1.4	14.7	1.0	33.4	49.6

In order to estimate the Ca/Si ratio and silicate linkage of C-S-H, the contribution of Si species from jennite needs to be accounted. According to literature [3, 7, 32, 43], the C-S-H formula can be assumed as  $(\text{CaO})_c \cdot \text{SiO}_2 \cdot (\text{H}_2\text{O})_{h+c}$ , where  $h$  ranges between 0.5 and 1.5 depending on the drying condition. The molar mass of C-S-H is therefore  $(60+18h+74c)$  g/mol. When expressed as  $(\text{CaO})_{1.5} \cdot \text{SiO}_2 \cdot (\text{H}_2\text{O})_{1.83}$ , the molar mass of jennite is 177 g/mol. Therefore, the molar ratio of jennite over C-S-H ( $m_s$ ) can be expressed as a function of  $c$  and  $h$ , (Eq. 3)

$$m_s = w_s \frac{60+18h+74c}{177} \quad (3)$$

where  $w_s$  is the mass ratio of jennite over C-S-H (Table 1). Many literatures have demonstrated that, for every unit mole of C-S-H with the formula  $(\text{CaO})_c \cdot \text{SiO}_2 \cdot (\text{H}_2\text{O})_{h+c}$ , the molar number of  $Q^I$  and  $Q^2_{p\_CSH}$  are  $(3c-2)$  and  $(2-2c)$ , respectively [6, 7, 14, 28, 32, 43]. Considering the molar number of  $Q^2_{p\_jennite}$  to be  $2m_s/3$ , the resulted overall molar ratio of  $Q^I$  signal over  $Q^2_p$  can be expressed as follows (Eq. 4),

$$\frac{Q^I\%}{Q^2_p\%} = \frac{3c-2}{2-2c+2m_s/3} \quad (4)$$

The combination of Eq. 3 and 4 readily leads to the solution of  $c$ , given three input data, i.e. 1) the mass ration between jennite and C-S-H, 2) the molar ratio between  $Q^I$  and  $Q^2_p$  signal, and 3)  $h$ . The first two data are listed in Table 1 and Table 2. As mentioned above,  $h$  usually varies between 0.5 and 1.5. Our calculation indicates that such a variation range only results in an uncertainty of 0.02 in the calculation of  $c$ .

Based on the above equations, the percentage of each silicate species from each Si-containing phases is calculated and listed in Table 3. The uncertainty in calculating the Ca/Si of C-S-H is estimated to be  $\pm 0.03$ . In D0, C-S-H contains significantly more  $Q^I$  than  $Q^2_p$  and  $Q^2_b$ , indicating a largely dimeric silicate chain. The estimated  $MCL$  (2.7) is in general accordance with reported data. The  $Q^2$  species dominate the C-S-H silicate chain in leached samples, leading to a significantly increased  $MCL$ . Minor amount of  $Q^3$  is

observed in the C-S-H in D1. In D4,  $Q^3$  is present in pronounced amount whereas the  $Q^1$  signal is nearly unobserved. Thus, via leaching the silicate linkage in C-S-H evolves from a largely dimeric configuration (D0) to a more continuously linked structure (D0.5), and to an increasingly crosslinked structure (D1, D4). Amorphous silica gel forms at high degree of decalcification (D1 and D4). As measured by ICP-AES, the bulk Ca/Si ratio is 1.38, 0.8, 0.62 and 0.3 for D0, D0.5, D1 and D4, respectively, which is consistent with the decalcification of C-S-H and the increasing amount of produced silica gel.

Table 3. The calculated percentage of Si species from each phase and the configuration information (Ca/Si,  $MCL$  and  $n_c$ ) of C-S-H.

	$Q^1_{CSH}$	$Q^2_{p\_CSH}$	$Q^2_{b\_CSH}$	$Q^3_{CSH}$	$Q^2_{p\_jennite}$	$Q^2_{b\_jennite}$	$Q^3_{Si\ gel}$	$Q^4_{Si\ gel}$	Ca/Si _CSH	$MCL$	$n_c$
D0	61.4	14.2	7.1	0	11.6	5.8	0	0	1.00	2.7	1.3
D0.5	24.7	34.9	17.5	0	15.3	7.7	0	0	0.78	6.2	1.7
D1	29.7	26.2	9.0	4.1	2.9	1.5	19.6	7.1	0.81	9.3	1.6
D4	1.4	14.7	1.0	6.4	0	0	27.0	49.6	0.69	68.5	2.2

### 3.3. High pressure X-ray diffraction study

The diffractogram as a function of applied hydrostatic pressure is shown in Figure 3. The C-S-H peaks as indicated in Figure 1a are here labeled with red dashed lines. The sample volume in HP-XRD experiment is so small that it is possible to avoid loading large crystal impurities into the sample chamber. As shown in Figure 3, the presence of jennite is observed in D0 and D0.5, whereas calcite is nearly unobserved in all measurements since it was not loaded into the sample chamber. Amorphous silica gel is observed in D4 at elevated pressure but not at ambient pressure (Figure 3c). This is due to the inhomogeneous distribution of silica gel in the sample chamber, such that it moved to the beam spot due to the deformation of the chamber when external load was applied.

The peak 1 of C-S-H are better resolved in HP-XRD compared with lab-XRD data. The peak 3 (C-S-H (200) diffraction) overlaps with the (120) peak of jennite [30] in D0 and

D0.5, but clearly resolved in D4. The peak 4 of C-S-H can be visually differentiated with the jennite ( $\bar{5}\bar{3}0$ ) peak at pressure lower than ~2 GPa, yet they overlap at higher pressure values. For all measured samples, the diffraction peaks move to the right-hand-side as pressure increases, indicating a monotonic decrease of inter-planar distance. A pressure-induced peak-broadening is observed as pressure increases, especially for peak 1. This is a common phenomenon in HP-XRD experiment due to the reduced ordering when the sample is compressed.

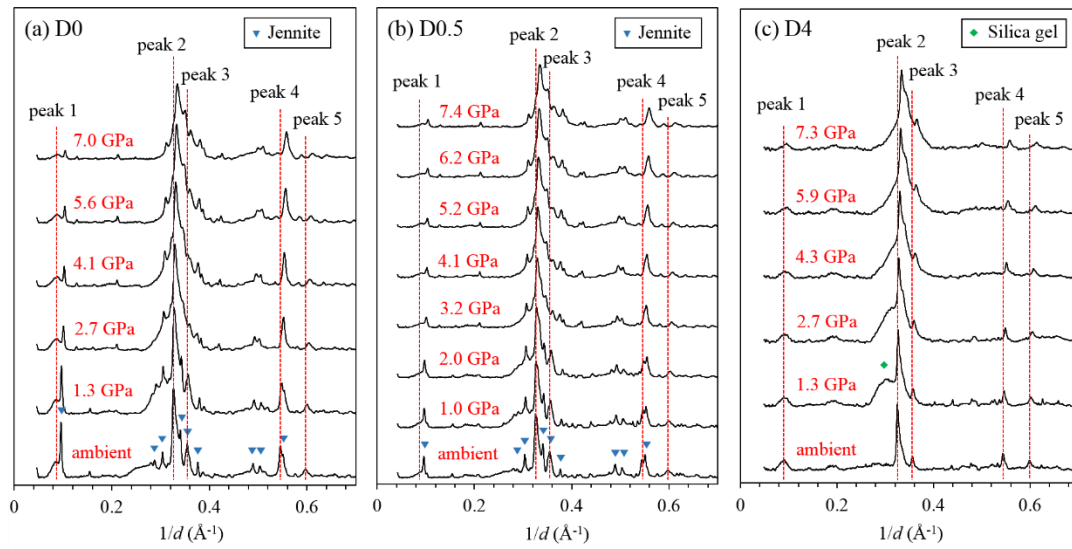


Figure 3. X-ray diffractogram of (a) D0, (b) D0.5 and (c) D4 as function of hydrostatic pressure. The C-S-H peaks are indicated with red-dotted lines. The impurities are labeled with blue-triangle (jennite) and green-diamond (amorphous silica gel) symbols.

Refinement of the HP-XRD data may result in eigenvalues of the strain tensor as a function of applied pressure, by comparing the unit cell parameters of the “original” and the “strained” unit cell. Previous HP-XRD studies of C-(A-)S-H have proven that the incompressibility within the C-(A-)S-H layer is almost independent of the silicate chain linkage [20, 21], and that the layer is rather isotropic along  $a$  and  $b$ -axis [44]. To validate such phenomena for the studied samples here, and to simplify the analysis from Rietveld Refinement on each XRD result, here the  $d$ -spacing of each C-S-H peak is directly obtained

from peak-fitting. To quantify the incompressibility along certain crystal direction, the compression strain of the corresponding  $d$ -spacing is calculated as  $\varepsilon = 1 - \frac{d}{d_0}$ , where  $d$  and  $d_0$  are the current and original  $d$ -spacing, respectively. Note that we did not intend to fit the position of peak 3 in D0 and D0.5, since it is strongly overlapped with jennite (120) diffraction and the intensity of peak 3 is much lower than the latter peak.

As shown in Figure 4a, the data points of peak 1 represent the deformation along  $c$ -axis. The data points for the peak 2-5, corresponding to the compression of the  $ab$ -plane structure, are highly comparable across all measured samples. This readily confirms that the C-S-H deformation isotropically along  $a$ - and  $b$ -axis. Through evaluating the slope of the data points in Figure 4a, the incompressibility along  $a(b)$ -axis lies within  $-1/260$  and  $-1/330$  GPa<sup>-1</sup> (dashed lines), which is highly consistent with previously reported data for C-(A-)S-H samples with various Ca/Si and Al/Si [20, 21].

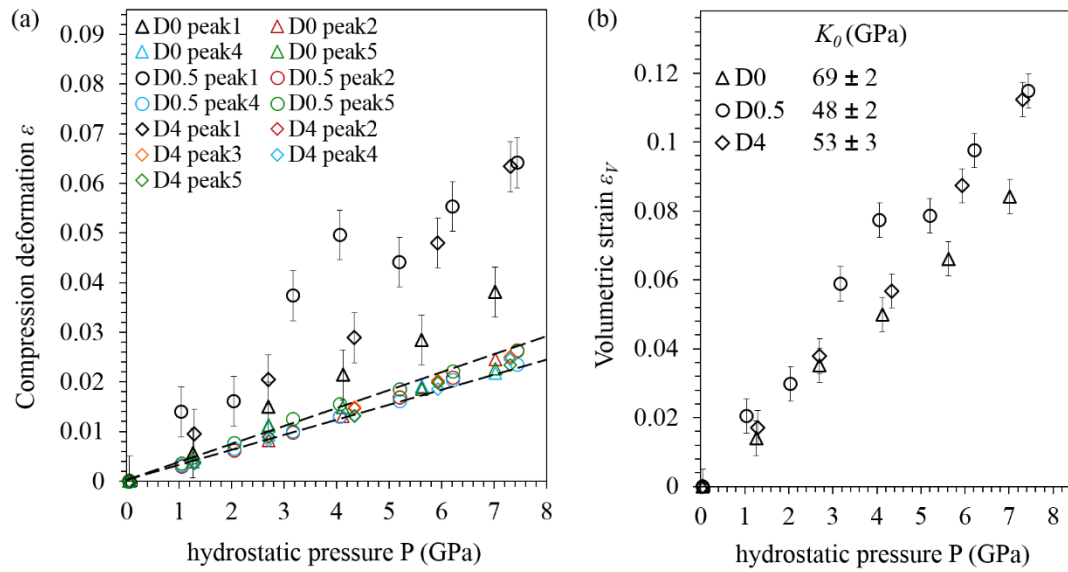


Figure 4. HP-XRD results of D0, D0.5 and D4: (a) the shortening of various  $d$ -spacing and (b) the volumetric strain as a function of hydrostatic pressure. The error bar illustrates the uncertainty from fitting peak position.

In terms of the *c*-axis, D0.5 and D4 share similar stiffness, and exhibit a shortening of ~6% at a hydrostatic pressure of ~7 GPa. This is roughly one time softer than the *c*-axis of D0 (~3.5% shortening at ~7 GPa), and two times softer than the *ab*-plane (~2% shortening at ~7 GPa). Therefore, the most significant change of C-S-H atomistic scale stiffness induced by decalcification is along the *c*-axis, whereas the stiffness within the layer stays rather constant, despite the strongly altered linkage of silicate dreierketten chain during decalcification.

The strain along *a*- and *b*-axis is estimated by averaging the inter-planar shortening corresponding to peaks 2-5. Within the studied deformation range, the volumetric strain  $\varepsilon_V$  is obtained simply by adding the strain along all three axes, as shown in Figure 4b. Using the 2<sup>nd</sup> order Birch-Murnaghan equation of state (Eq. 5), the bulk moduli  $K_0$  of D0, D0.5 and D4 are fitted as  $69 \pm 2$ ,  $48 \pm 2$  and  $53 \pm 3$  GPa, respectively.

$$P = \frac{3}{2}K_0((1 - \varepsilon_V)^{-\frac{7}{3}} - (1 - \varepsilon_V)^{-\frac{5}{3}}) \quad (5)$$

The stiffness along *c*-axis in D0.5 (non-crosslinking) and D4 (crosslinking) are generally comparable, yet D0.5 seems more compliant than D4 along *c*-axis when pressure is below 5 GPa (Figure 4a). This may indicate that the crosslinking in D4 contributes to a slight stiffening along *c*-axis, as also observed in a previous study on a crosslinked C-A-S-H sample [20]. Interestingly, at the pressure of 5 GPa the deformation of D0.5 along *c*-axis seems retrieved. Whereas beyond 5 GPa its deformation follows the same trend line as D4. So far, we do not have a solid explanation to this phenomenon. A possible reason might be that the pressure value around 5 GPa initiates a rearrangement of interlayer atoms in D0.5. Such rearrangement might be, for example, a bridging site silicate crosslinking. Further chemical analysis at elevated pressure is needed to validate such hypothesis.



#### 4. Discussion and conclusions

In all three decalcified C-S-H structures, the Ca/Si ratios seem to stabilize at 0.7-0.8. The (002) basal spacing slightly decreases from 11.7 Å before decalcification to 11.2-11.3 Å after decalcification. As shown in Figure 3, the (002) diffraction peaks of all measured samples are broad and of low intensity, indicating that the crystallite size before and after decalcification remains 2-3 layers along the *c*-axis. The C-S-H (002) peak of D0.5 is less intensive than in D0, whereas it is more renowned in D4. Decalcification increases the *MCL* from 2.7 (before decalcification) to longer than 6 even when using NH<sub>4</sub>NO<sub>3</sub> with the lowest concentration (0.5 mol/L). A further increase of the NH<sub>4</sub>NO<sub>3</sub> concentration to 4 mol/L significantly induces crosslinking of adjacent deirerketten chain. These evidences suggest a slight shortening in the interlayer distance, accompanied by a more disordered layer-stacking when D0 is decalcified to D0.5. The C-S-H crosslinking in D4 does not result in clear change in basal spacing, yet it seems to increase the layer stacking order compared with in D0.5.

Despite changes in chemical composition, the stiffness within the calcium silicate layer remains unchanged. Our previous work demonstrated that the in-planar (along *a*- and *b*-axis) stiffness of the C-S-H layer is mainly attributed to the intralayer CaO<sub>7</sub> polyhedron. The silicate dreierketten chain is rather compliant since it deforms by changing dihedral angle instead by shortening the Si-O bond [21]. Therefore, the HP-XRD study here strongly indicates that the intralayer Ca is not leached out during decalcification, since otherwise the in-planar stiffness of decalcified C-S-H would significantly decrease.

The basic building unit of the tobermorite-like layer structure is three silicate tetrahedra combining two intralayer Ca polyhedra (i.e. C<sub>2</sub>S<sub>3</sub>), plus a variable amount of interlayer content [45, 46]. With the data in Table 3, the basic building unit (neglecting water) of the studied C-S-H samples are calculated as C<sub>2.2</sub>S<sub>2.2</sub>, C<sub>2.0</sub>S<sub>2.6</sub>, C<sub>2.0</sub>S<sub>2.5</sub>, and C<sub>2.0</sub>S<sub>2.9</sub> for D0, D0.5,

D1 and D4, respectively. Despite the two intralayer Ca, the amount of interlayer Ca per basic unit is 0.2 for D0 and zero for all the leached samples. A schematic evolution of the atomistic configuration is shown in Figure 5. According to our previous study [21], C-S-H stiffens when the interlayer region is densified with Ca ions. From D0 to D0.5, the C-S-H interlayer Ca essentially all leaches out while the interlayer distance is shortened by only ~10%. This may explain the softening of C-S-H in D0.5 along the *c*-axis compared with C-S-H in D0. On the other hand, the bulk modulus of C-S-H in D4 is slightly higher than that in D0.5. This suggests that a crosslinking in the interlayer region may also stiffen the *c*-axis of C-S-H, as also observed in the Al-induced crosslinking in C-A-S-H [20].

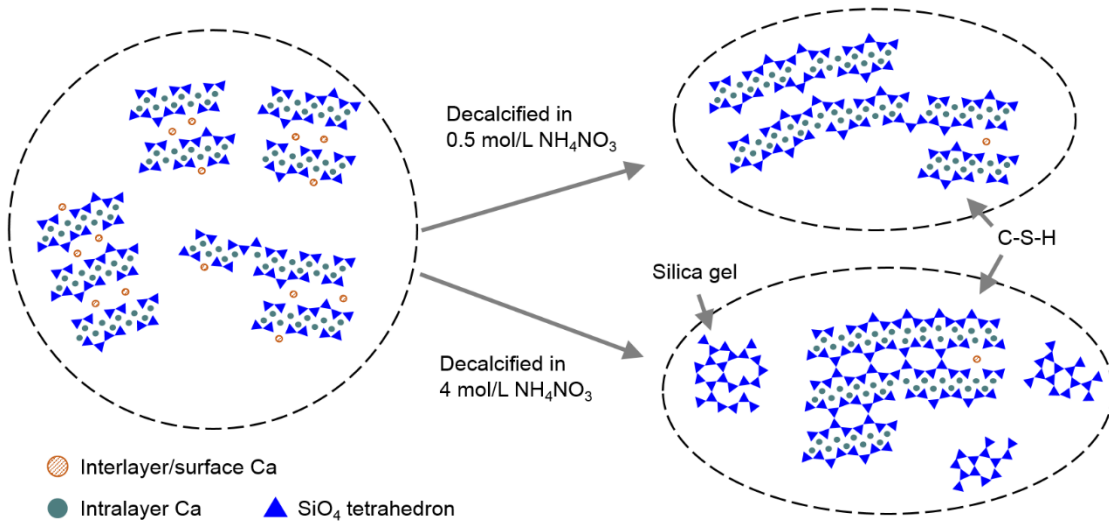


Figure 5. An illustration of the atomistic structural evolution of C-S-H undergoing decalcification using  $\text{NH}_4\text{NO}_3$  solution.

In a more realistic chemical boundary condition of concrete leaching, the leaching agent might be constantly renewed such that the configuration change of C-S-H may follow a different path compared with the current study. A recent C-S-H leaching study in an open flow-reactor seems to suggest no polymerization of silicate chain during leaching [8]. According to our result, the Si linkage is less dominant to the C-S-H bulk modulus, compared with the interlayer Ca content. Therefore the bulk modulus of decalcified C-S-

H in an open system scenario is expected to reach a constant value as soon as all the interlayer Ca leaches out. HP-XRD study of these samples may provide further validation. We summarize our conclusions as follows.

- 1) Decalcification using 0.5 mol/L  $\text{NH}_4\text{NO}_3$  solution leads to the leaching of C-S-H interlayer Ca and the increased linkage of its silicate chain. Under higher  $\text{NH}_4\text{NO}_3$  concentration, C-S-H crosslinking and amorphous silica gel formation are observed.
- 2) The interlayer Ca completely leaches out in all decalcified samples. As long as C-S-H maintains its tobermorite-like layer structure during decalcification, the intralayer Ca does not leach out. Further decalcification takes place by a complete dissolution of C-S-H.
- 3) The mechanical property of C-S-H remains generally unchanged within the calcium silicate layer, despite the vast change of silicate linkage. The stiffness along the *c*-axis (perpendicular to the layer) is clearly reduced due to the leaching of interlayer Ca. This may lead to a bulk modulus reduction as much as 30%, i.e. from 69 GPa (Ca/Si ~ 1.0, before decalcification) to around 50 GPa (Ca/Si ~ 0.7-0.8, after decalcification).
- 4) Under more severe decalcification condition (D4), the crosslinking in C-S-H interlayer slightly increase the bulk modulus of C-S-H, compared with decalcified but non-crosslinked C-S-H (D0.5).

## **Acknowledgement**

This study was funded by National Natural Science Foundation of China (Grant No.51678219), Fundamental Research Funds for the Central Universities (Grant No.2018B14214). G. Geng wants to acknowledge the European Union's Horizon 2020 research and innovation programme under the Marie Skłodowska-Curie grant agreement No 701647. Dr. Dominik Daisenberger and Dr. Annette Kleppe are acknowledged for

setting up the high-pressure XRD experiments in beamline I15 of Diamond Light Source.

Prof. Paulo Monteiro is acknowledged for insightful discussion about the research plan.

The authors declare that they have no conflict of interest.

## Reference

1. H.F. Taylor, Proposed structure for calcium silicate hydrate gel, *J. Am. Ceram. Soc.* 69 (1986) 464-467.
2. P.K. Mehta, P.J. Monteiro, *Concrete Microstructure, Properties, and Materials*, 4<sup>th</sup> edition, McGraw-Hill Companies, New York City, 2014.
3. J.J. Thomas, J.J. Chen, H.M. Jennings, A.N. Dan, Ca-OH Bonding in the C-S-H gel phase of tricalcium silicate and white Portland cement pastes measured by inelastic neutron scattering, *Chem. Mater.* 15 (2003) 3813-3817.
4. D. Gawin, F. Pesavento, B.A. Schrefler, Modeling deterioration of cementitious materials exposed to calcium leaching in non-isothermal conditions, *Comput. Methods in Appl. Mech. Eng.* 198 (2009) 3051.
5. K. Haga, M. Shibata, M. Hironaga, S. Tanaka, S. Nagasaki, Silicate anion structural change in calcium silicate hydrate gel on dissolution of hydrated cement, *J. Nucl. Sci. Tech.* 39 (2002) 540-547.
6. J.J. Chen, J.J. Thomas, H. M. Jennings, Decalcification shrinkage of cement paste, *Cem. Concr. Res.* 36 (2006) 801-809.
7. J.J. Chen, J.J. Thomas, H.F.W. Taylor, H.M. Jennings, Solubility and structure of calcium silicate hydrate, *Cem. Concr. Res.* 34 (2004) 1499-1519.
8. N.C. Marty, S. Grangeon, F. Warmont, C. Lerouge. Alteration of nanocrystalline calcium silicate hydrate (CSH) at pH 9.2 and room temperature: a combined mineralogical and chemical study. *Mineral. Mag.* 79 (2015) 437-458.

9. F.P. Glasser, J. Marchand, E. Samson, Durability of concrete—degradation phenomena involving detrimental chemical reactions, *Cem. Concr. Res.* 38 (2008) 226-246.
10. I. Segura, M. Molero, S. Aparicio, J.J. Anaya, A. Moragues, Decalcification of cement mortars: characterisation and modelling. *Cem. Concr. Comp.* 35 (2013) 136-150.
11. J.J. Kim, M.K. Rahman, M.M.R. Taha, Examining microstructural composition of hardened cement paste cured under high temperature and pressure using nanoindentation and Si MAS NMR, *App. Nanosci.* 2 (2012) 445-456.
12. J.J. Beaudoin, L. Raki, R. Alizadeh, A Si MAS NMR study of modified C–S–H nanostructures, *Cem. Concr. Comp.* 31 (2009) 585-590.
13. G.L. Saoût, E. Lécolier, A. Rivereau, Z. Hélène, Chemical structure of cement aged at normal and elevated temperatures and pressures, Part II: Low permeability class G oilwell cement, *Cem. Concr. Res.* 36 (2006) 428-433.
14. R.J. Myers, J.L. Provis, B. Lothenbach, Composition-solubility-structure relationships in calcium (alkali) aluminosilicate hydrate (C-(N, K-)A-S-H), *Dalton Trans.* 44 (2015) 13530-13544.
15. J.J. Kim, E.M. Foley, M.M.R. Taha, Nano-mechanical characterization of synthetic calcium-silicate-hydrate (C-S-H) with varying CaO/SiO<sub>2</sub> mixture ratios, *Cem. Concr. Comp.* 36 (2013) 65-70.
16. G. Constantinides, F.J. Ulm, The effect of two types of C-S-H on the elasticity of cement-based materials: Results from nanoindentation and micromechanical modeling, *Cem. Concr. Res.* 34 (2004) 67-80.
17. J.J. Gaitero, W. Zhu, I. Campillo, Multi-scale study of calcium leaching in cement pastes with silica nanoparticles, *Nanotech. Constr.* 3 (2009) 193-198.

18. R.J.M. Pellenq, A. Kushima, R. Shahsavari, K.J. Van Vliet, M.J. Buehler, S. Yip, F.J. Ulm, A realistic molecular model of cement hydrates, *Proc. Natl. Acad. Sci. USA.* 106 (2009) 16102-16107.
19. M.A. Qomi, K.J. Krakowiak, M. Bauchy, K.L. Stewart, R. Shahsavari, D. Jagannathan, D.B. Brommer, A. Baronnet, M.J. Buehler, S. Yip, F.J. Ulm, Combinatorial molecular optimization of cement hydrates, *Nat. Commun.* 5 (2014) 4960.
20. G. Geng, R.J. Myers, J. Li, R. Maboudian, C. Carraro, D.A. Shapiro, P.J.M. Monteiro, Aluminum-induced dreierketten chain cross-links increase the mechanical properties of nanocrystalline calcium aluminosilicate hydrate, *Sci. Rep.* 7 (2017) 44032.
21. G. Geng, R.J. Myers, M.J.A. Qomi, P.J.M. Monteiro, Densification of the interlayer spacing governs the nanomechanical properties of calcium-silicate-hydrate, *Scientific Reports.* 7 (2017) 10986.
22. E. L'Hôpital, B. Lothenbach, K. Scrivener, D.A. Kulik, Alkali uptake in calcium alumina silicate hydrate (C-A-S-H), *Cem. Concr. Res.* 85 (2016) 122-136.
23. R.J. Myers, E. L'Hôpital, J.L. Provis, B. Lothenbach, Effect of temperature and aluminium on calcium (alumino) silicate hydrate chemistry under equilibrium conditions, *Cem. Concr. Res.* 68 (2015) 83-93.
24. E.M. Foley, J.J. Kim, M.M.R. Taha, Synthesis and nano-mechanical characterization of calcium-silicate-hydrate (C-S-H) made with 1.5 CaO/SiO<sub>2</sub> mixture. *Cem. Concr. Res.* 42 (2012) 1225-1232.
25. J.J. Thomas, Effects of decalcification on the microstructure and surface area of cement and tricalcium silicate paste, *Cem. Concr. Res.* 34 (2004) 2297-2307.
26. S. Kamali, M. Moranville, S. Leclercq, Material and environmental parameter effects on the leaching of cement pastes: experiments and modelling, *Cem. Concr. Res.* 38 (2008) 575-585.

27. C. Sun, L. Liu, Y. Du, Analyses of decalcification process of calcium silicate hydrate (C-S-H) phase, Proceeding of the 2<sup>nd</sup> International Seminar on Materials Science and Application (SMSA2018), Shanghai, 2008.
28. I.G. Richardson, Tobermorite/jennite- and tobermorite/calcium hydroxide-based models for the structure of C-S-H: applicability to hardened pastes of tricalcium silicate, h-dicalcium silicate, Portland cement, and blends of Portland cement with blast-furnace slag, metakaolin, or silica fume, *Cem. Concr. Res.* 34 (2004) 1733-1777.
29. L. Lutterotti, Maud: a Rietveld analysis program designed for the internet and experiment integration. *Acta Crystallogr., Sect. A: Found. Crystallogr.* 56 (2000) S54.
30. E. Bonaccorsi, S. Merlino, H.F.W. Taylor, The crystal structure of jennite,  $\text{Ca}_9\text{Si}_6\text{O}_{18}(\text{OH})_6 \cdot 8\text{H}_2\text{O}$ . *Cem. Concr. Res.* 34 (2004) 1481-1488.
31. S.A. Markgraf, R.J. Reeder, High-temperature structure refinements of calcite and magnesite, *Am. Mineral.* 70 (1985) 590-600.
32. I.G. Richardson, Model structures for C-(A)-S-H (I). *Acta Cryst. B* 70 (2014) 903-923.
33. S. Merlino, E. Bonaccorsi, E., T. Armbruster, The real structure of tobermorite 11Å: normal and anomalous forms, OD character and polytypic modifications. *Europ. J. Mineral.* 13 (2001) 577-590.
34. E. Bonaccorsi, S. Merlino, A.R. Kampf, The crystal structure of tobermorite 14 Å (plombierite), a C-S-H phase. *J. Am. Ceram. Soc.* 88 (2005) 505-512.
35. K. Garbev, G. Beuchle, M. Bornefeld, L. Black, P. Stemmermann, Cell dimensions and composition of nanocrystalline calcium silicate hydrate solid solutions. Part 1: synchrotron-based X-ray diffraction. *J. Am. Ceram. Soc.* 91 (2008), 3005-3014.
36. S. Grangeon, F. Claret, Y. Linard, C. Chiaberge, X-ray diffraction: a powerful tool to probe and understand the structure of nanocrystalline calcium silicate hydrates, *Acta Cryst. B.* 69 (2013) 465-473.

37. R. Letoullec, J.P. Pinceaux, P. Loubeyre, The membrane diamond anvil cell: a new device for generating continuous pressure and temperature variations, *Int. Journal of High Pressure Res.* 1 (1988) 77-90.
38. C. Prescher, V.B. Prakapenka, DIOPTAS: a program for reduction of two-dimensional X-ray diffraction data and data exploration, *High Pressure Res.* 35 (2015) 223-230.
39. R.W. Cheary, A.A. Coelho, Programs XFIT and FOURYA, deposited in CCP14 Powder Diffraction Library, Engineering and Physical Sciences Research Council, Daresbury Laboratory, Warrington, England, <http://www.ccp14.ac.uk/tutorial/xfit-95/xfit.htm>, (1996).
40. V.A. Drits, C. Tchoubar, X-ray diffraction by disordered lamellar structures: Theory and applications to microdivided silicates and carbons, Springer Science & Business Media, Berlin, 2012.
41. R.J. Myers, S.A. Bernal, R. San Nicolas, J.L. Provis, Generalized structural description of calcium-sodium aluminosilicate hydrate gels: the cross-linked substituted tobermorite model, *Langmuir*. 29 (2013) 5294-5306.
42. Y. He, L. Lu, L.J. Struble, J.L. Rapp, P. Mondal, S. Hu, Effect of calcium-silicon ratio on microstructure and nanostructure of calcium silicate hydrate synthesized by reaction of fumed silica and calcium oxide at room temperature, *Mater. Struct.* 47 (2014) 311-322.
43. C.S. Walker, S. Sutou, C. Oda, M. Mihara, A. Honda, Calcium silicate hydrate (CSH) gel solubility data and a discrete solid phase model at 25 °C based on two binary non-ideal solid solutions, *Cem. Concr. Res.* 79 (2016) 1-30.
44. G. Geng, R.N. Vasin, J. Li, M.J.A. Qomi, J. Yan, H.R. Wenk, P.J. Monteiro, Preferred orientation of calcium aluminosilicate hydrate induced by confined compression, *Cem. Concr. Res.* 113 (2018) 186-196.



45. A.K. Mohamed, S.C. Parker, P. Bowen, S. Galmarini, An atomistic building block description of CSH-Towards a realistic CSH model, *Cem. Concr. Res.* 107 (2018) 221-235.
46. G.D. Miron, Internally consistent thermodynamic database for fluid-rock interaction: tools, methods and optimization, Doctoral dissertation, ETH Zurich, 2016, chapter 2A. DOI: <https://doi.org/10.3929/ethz-a-010655112>.